

Probing the Neutral Fraction of the IGM with GRBs during the Epoch of Reionisation

Matthew McQuinn^{1*}, Adam Lidz¹, Matias Zaldarriaga^{1,2}, Lars Hernquist¹,
Suvendra Dutta¹

¹ *Harvard-Smithsonian Center for Astrophysics, 60 Garden St., Cambridge, MA 02138*

² *Jefferson Laboratory of Physics, Harvard University, Cambridge, MA 02138*

5 August 2021

ABSTRACT

We show that near-infrared observations of the red side of the Ly α line from a single gamma ray burst (GRB) afterglow cannot be used to constrain the global neutral fraction of the intergalactic medium (IGM), \bar{x}_H , at the GRB’s redshift to better than $\delta\bar{x}_H \sim 0.3$. Some GRB sight-lines will encounter more neutral hydrogen than others at fixed \bar{x}_H owing to the patchiness of reionisation. GRBs during the epoch of reionisation will often bear no discernible signature of a neutral IGM in their afterglow spectra. We discuss the constraints on \bar{x}_H from the $z = 6.3$ burst, GRB050904, and quantify the probability of detecting a neutral IGM using future spectroscopic observations of high-redshift, near-infrared GRB afterglows. Assuming an observation with signal-to-noise similar to the Subaru FOCAS spectrum of GRB050904 and that the column density distribution of damped Ly α absorbers is the same as measured at lower redshifts, a GRB from an epoch when $\bar{x}_H = 0.5$ can be used to detect a partly neutral IGM at 97% confidence level $\approx 10\%$ of the time (and, for an observation with three times the sensitivity, $\approx 30\%$ of the time).

Key words: cosmology: theory – intergalactic medium – galaxies: high redshift

1 INTRODUCTION

Tomorrow, a gamma ray burst (GRB) may be observed that originates from the death of one of the first stars, during the epoch of reionisation. Despite the great distance to this burst, it will be the brightest gamma ray source on the sky for several tens of seconds, one of the brightest cosmological X-ray sources for hours, and its afterglow will be observable for weeks in the near-infrared (and, for the first few hours, brighter than any $z \sim 6$ QSO). Much of the optical and near-infrared light will be obscured by the Ly α forest, and this obscuration will enable the strongest constraint to date on the neutral hydrogen fraction of the intergalactic medium (IGM) at the burst’s redshift.

In fact, such an occurrence may already have been realised. Haislip et al. (2006), Kawai et al. (2006), Tagliaferri et al. (2005), and Totani et al. (2006) observed and analysed the optical/near-infrared afterglow of GRB050904, identified to be at $z = 6.3$ – possibly during the reionisation epoch and the GRB with the highest con-

firmed redshift. Totani et al. (2006) derived the constraint on the global neutral fraction $\bar{x}_H < 0.6$ at $z = 6.3$. In this paper, we discuss the assumptions that went into their analysis, and we investigate how realistic modelling of reionisation can affect constraints on \bar{x}_H from GRB050904 and from future $z > 6$ GRBs.

The Swift satellite has greatly increased the sample of GRBs with known redshifts in the last two years (Gehrels et al. 2004). Future missions such as EXIST (Grindlay & The Exist Team 2006) and JWST (Gardner et al. 2006) will further enhance our ability to detect high-redshift GRBs and will enable more detailed follow-up studies of their near-infrared afterglows. Interestingly, approximately one-half of Swift bursts are “dark bursts” – bursts that have detected X-ray afterglows, but that have no measurable optical emission (e.g., Fillard et al. 2006). While it is probable that most dark bursts originate from low-redshift, dust-rich galaxies, a fraction of dark bursts may originate from $z > 6$ and are “dark” because Ly α absorption from the high-redshift IGM absorbs the optical emission (e.g., Malesani et al. 2005).

In addition to their extreme luminosity, there are several

* mmcquinn@cfa.harvard.edu

other advantages to studying reionisation with GRBs compared to other probes of this epoch. First, the afterglows of high-redshift GRBs are observed at earlier (brighter) times in the source frame than those at lower redshifts, so the dimming owing to increased luminosity distance is nearly cancelled, and the observed flux is almost independent of redshift (Lamb & Reichart 2001; Ciardi & Loeb 2000). Second, unlike the spectra of galaxies and quasars, the intrinsic afterglow spectrum of a GRB is a featureless power-law at the relevant wavelengths, allowing a more precise measurement of absorption owing to a neutral IGM (Barkana & Loeb 2004). Finally, since the theoretical expectation is that most of the star formation at $z \gtrsim 6$ occurs in halos with $m \sim 10^9 M_\odot$ and because observations at $z \gtrsim 6$ currently probe only the most massive galaxies and QSOs ($m \gtrsim 10^{11} M_\odot$), high-redshift GRB host galaxies should be less massive than galaxies selected in another manner. Consequently, GRB host galaxies will sit in smaller HII regions during reionisation (on average) than galaxies selected by different means. Therefore, GRBs will suffer a larger Ly α IGM absorption feature.

In this work, we do not concentrate on wavelengths blueward of source-frame Ly α (in the Ly α forest) to derive constraints from GRBs. Any blueward flux indicates the presence of ionised gas at the redshift of the transmission. However, at high redshifts there is little or no flux in the Ly α forest, even in ionised regions, owing to the increase in density with increasing redshift, the decrease in the size and in the number of voids, and the decrease in the amplitude of the ionising background (e.g., Becker et al. 2007 and Lidz et al. 2007). As a result, it is difficult to distinguish a partly ionised IGM from a fully ionised one with the $z > 6$ forest (Becker et al. 2007; Lidz et al. 2007). Future observations of the $z > 6$ Ly α forest from additional QSOs and GRBs will aid reionisation studies, but it is unclear whether such studies will ever provide definitive evidence for neutral pockets in the IGM. In contrast, the shape of the line profile redward of Ly α is sensitive to a substantially neutral IGM and, therefore, can be used to unambiguously detect reionisation (Miralda-Escude 1998).

Little is known about the rate of GRBs at $z > 6$. We assume that the rate of long GRBs traces the massive star formation rate (SFR) for most calculations in this work.¹ The assumption that the GRB rate traces the massive SFR is supported by observations of lower redshift GRB host galaxies (Bloom et al. 2002; Djorgovski et al. 2001). However, Kistler et al. (2008) found that the GRB rate is four times higher at $z \approx 4$ than if the GRB rate exactly traces the SFR. Other properties of a galaxy apart from its massive SFR might be correlated with its rate of GRBs. For example, Stanek et al. (2006) found that $z < 0.25$ GRBs – GRBs that are typically under-luminous – are preferentially in metal-poor galaxies.

Making the assumption that the GRB rate traces the observed SFR, Salvaterra et al. (2008) predicted that SWIFT will be triggered by 1 – 4 bursts a year above $z = 6^2$ and that the EXIST mission would observe 10 – 60

bursts a year. Other studies have predicted even larger rates (Bromm & Loeb 2002; Daigne et al. 2006).

At $z > 6$, POPIII stars with average masses of $\sim 100 M_\odot$ may exist. It is unclear whether the death of a POPIII star can result in a GRB. Fryer et al. (2001) identified a mechanism that might produce GRBs from POPIII stars. However, once the interstellar metallicity reaches a critical value of $\sim 10^{-3.5}$ solar in a high-redshift galaxy, POPIII star formation quenches and the normal mode of POPII star formation begins (e.g., Mackey et al. 2003; Yoshida et al. 2004), and this mode is known to produce GRBs. Most if not all of reionisation likely owes to photons from POPII-like stars (e.g., Sokasian et al. 2004; Trac & Cen 2007).

In Section 2, we discuss the absorption profiles of a neutral IGM as well as of a damped Ly α absorber (DLA), and, in Section 3, we discuss our simulations of reionisation and their implications for the amount of IGM absorption in a GRB afterglow spectrum. Section 4 quantifies the detectability of a neutral IGM from GRB afterglow spectra, and Section 5 describes the constraints on \bar{x}_H from the $z = 6.3$ burst, GRB050904. For our calculations, we adopt a cosmology with $\Omega_m = 0.27$, $\Omega_\Lambda = 0.73$, $\Omega_b = 0.46$, $\sigma_8 = 0.8$, $n = 1$, and $h = 0.7$, which is consistent with the most recent cosmic microwave background and large scale structure data (Spergel et al. 2007). We express all distances in comoving units unless otherwise noted.

When this project was nearing completion, we learned of a similar effort by Mesinger & Furlanetto (2007) and refer the reader there for a complementary discussion.

2 THE RED DAMPING WING

In the standard picture, GRB afterglows result from shells of relativistic matter colliding with the interstellar medium, shocking, and radiating via synchrotron emission (Sari et al. 1998). The observed flux of a GRB just redward of GRB-frame Ly α is given roughly by $\mathcal{F} = A (\nu/\nu_\alpha)^{-\beta} \exp[-\tau_\alpha(\nu)]$, where A is a time-dependent amplitude, β is a time-dependent power-law index, ν_α is the frequency at the Ly α line centre, and

$$\begin{aligned} \tau_\alpha(\nu) \approx & \int_0^{z_g} \frac{dz}{1+z} \frac{c}{H(z)} n_H(z) \sigma_\alpha \left(\nu_z \left(1 + \frac{v(z)}{c} \right) \right) \\ & + N_{\text{HI}} \sigma_\alpha \left(\nu_{z_{\text{DLA}}} \left(1 + \frac{v(z_{\text{DLA}})}{c} \right) \right). \end{aligned} \quad (1)$$

Here, $\nu_z \equiv \nu (1+z)$, $z_g [z_{\text{DLA}}]$ is the redshift of the GRB host galaxy [DLA], $\sigma_\alpha(\nu)$ is the Lorentzian-like Ly α naturally broadened scattering cross section at frequency ν , and $v(z)$ is the line-of-sight peculiar velocity of the gas. The first term on the right-hand side of Equation (1) owes to IGM absorption and the second owes to absorption by a DLA with column density N_{HI} . The extended absorption profile redward of Ly α shaped by the factor $\exp[-\tau_\alpha(\nu)]$ is commonly referred to as the “damping wing”.

Let us first ignore absorption owing to a DLA and the

¹ We do not consider the other class of GRBs, the “short” GRBs, in this study. These bursts, while still cosmological, are more local than long GRBs and typically do not have a detected afterglow.

² This rate is larger than the SWIFT rate of 1 identified $z > 6$

bursts in three years, but it is possible that these numbers can be reconciled in light of these dark bursts.

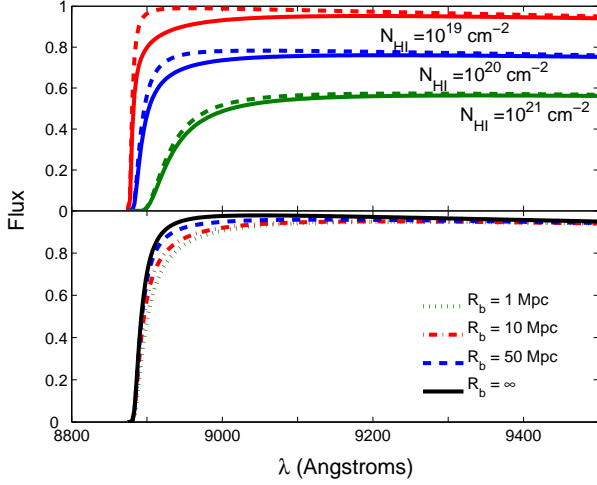


Figure 1. Illustration of the GRB afterglow flux near the GRB-frame Ly α wavelength. The top panel depicts the afterglow flux for both an ionised universe (dashed curves) and with $\bar{x}_H = 0.5$ and $R_b = 10$ Mpc (solid curves). The bottom panel illustrates the effect of bubble size on the afterglow flux, assuming $\bar{x}_H = 0.5$ and $N_{\text{HI}} = 10^{20} \text{ cm}^{-2}$. The normalisation of the flux in these panels is arbitrary, and it has been adjusted in the top panel to separate the sets of curves. These curves are calculated with $\beta = 1.25$ and $z_g = 6.3$, and λ is the observed wavelength.

effects of peculiar velocities. For an isolated bubble of co-moving size R_b in a homogeneous medium with neutral fraction \bar{x}_H , Equation (1) simplifies to the expression (e.g., Loeb & Rybicki 1999)

$$\tau_\alpha(\nu) \approx 900 \text{ km s}^{-1} \times \bar{x}_H \left(\frac{1+z_g}{8} \right)^{3/2} \times \left(\frac{H(z_g) R_b}{(1+z_g)} - c \frac{\nu_z - \nu_\alpha}{\nu_\alpha} \right)^{-1}, \quad (2)$$

or $\tau(\nu_\alpha/(1+z_g)) \approx \bar{x}_H$ for a 1 proper Mpc bubble, noting that $H(z_g = 7) \approx 900 \text{ km s}^{-1} \text{ proper Mpc}^{-1}$.³ The width of the damping wing feature from a neutral IGM (defined here as the wavelength for which $\exp[-\tau_\alpha(\nu)] < 0.9$) is $\approx 25 (1+z_g) \text{ \AA}$. The width of this feature is typically broader than the feature due to a DLA, which falls off as $\Delta\lambda_\alpha^{-2}$ rather than the $\Delta\lambda_\alpha^{-1}$ scaling for IGM absorption, where $\Delta\lambda_\alpha$ is the difference between a given wavelength and that of Ly α in the GRB-frame (Miralda-Escude 1998).

Figure 1 illustrates the effect of the column density of the DLA (top panel) and the size of the HII region (bottom panel) on the absorption feature. Here we adopt the same simplistic parameterisation as in Equation (2): an HII region of size R_b surrounded by a homogeneously neutral IGM with neutral fraction \bar{x}_H . The dashed lines in the top panel represent an IGM with $\bar{x}_H = 0$, and the solid lines represent the case with $\bar{x}_H = 0.5$ and $R_b = 10$ Mpc. IGM absorption

produces a wider feature than that from a DLA. However, it becomes hard to visually discern absorption owing to a neutral IGM for $N_{\text{HI}} \gtrsim 10^{21} \text{ cm}^{-2}$. This illustration suggests that it is difficult to measure \bar{x}_H from GRB050904, which has $N_{\text{HI}} \approx 10^{21.6} \text{ cm}^{-2}$ (Totani et al. 2006). We return to this point in Section 5.

DLAs with $N_{\text{HI}} > 10^{19} \text{ cm}^{-2}$ are associated with all but one GRB for which N_{HI} has been measured (Chen et al. 2007). The cumulative distribution of N_{HI} for the current sample of ≈ 30 GRB DLAs scales as $N_{\text{HI}}^{0.3}$ between 10^{18} and $10^{21.5} \text{ cm}^{-2}$, and about half of all GRBs for which N_{HI} has been measured have $N_{\text{HI}} > 10^{21.5} \text{ cm}^{-2}$ (Chen et al. 2007). However, it is not clear how N_{HI} should scale with redshift. It is plausible that, since the average galaxy becomes less massive with redshift, $z > 6$ galaxies should, on average, have weaker DLAs. For galaxies to reionise the Universe, the escape fraction of ionising photons must be appreciable, implying that sight-lines with $N_{\text{HI}} \lesssim 10^{18} \text{ cm}^{-2}$ must exist.⁴

The bottom panel in Figure 1 depicts the effect of bubble size on the GRB afterglow spectrum. The IGM absorption for GRBs in bubbles with sizes between 1-10 Mpc is comparable. However, if the GRB sits in a large bubble with $R_b \sim 50$ Mpc, the absorption is strongly diminished. When $\bar{x}_H = 0.2$, roughly half of the skewers from GRBs in our simulations of reionisation sit in HII regions that are larger than 50 Mpc (Section 3).

3 EFFECT OF PATCHY REIONISATION

While the GRB itself does not ionise the IGM around it, earlier star formation from its host and neighbouring galaxies can grow a large HII region. To model reionisation around a GRB, we employ three radiative transfer simulations that are each 186 Mpc on a side. These simulations are post-processed on a 1024^3 particle N-body field. Unresolved halos are included with extended Press-Schechter merger trees. These three simulations are described in detail in McQuinn et al. (2007b) [and the methodology is described in McQuinn et al. (2007a)], and they are meant to span the range of plausible morphologies for reionisation by galaxies. Here is a brief description of the models for the sources and sinks of ionising photons used in each of the three simulations:

Model (i): All halos above the mass at which the gas can cool atomically (m_{cool}) contribute ionising photons at a rate that is proportional to their mass m . The scaling $\dot{N}_{\text{ion}} \sim m$ assumes that the massive SFR is proportional to the amount of gas within a galaxy.

Model (ii): Halos more massive than m_{cool} contribute to the production of ionising photons, with the ionising luminosity of the sources scaling as halo mass to the 5/3 power. This scaling is chosen to match the relationship between star formation efficiency and galaxy mass that is observed in low-redshift dwarf galaxies (Kauffmann et al. 2003) as well as the SFR found in theoretical studies that include supernova feedback (Dekel & Woo 2003; Hernquist & Springel 2003; Springel & Hernquist 2003).

³ To derive Equation (2), approximate $\sigma_\alpha(\nu)$ with a Lorentzian profile and ignore the redshift dependence that appears in the numerator of the integrand in Equation (1). We have checked that these approximations are accurate to better than 10% for relevant R_b .

⁴ An optical depth of unity at the HI Lyman-limit requires $N_{\text{HI}} = 2 \times 10^{17} \text{ cm}^{-2}$.

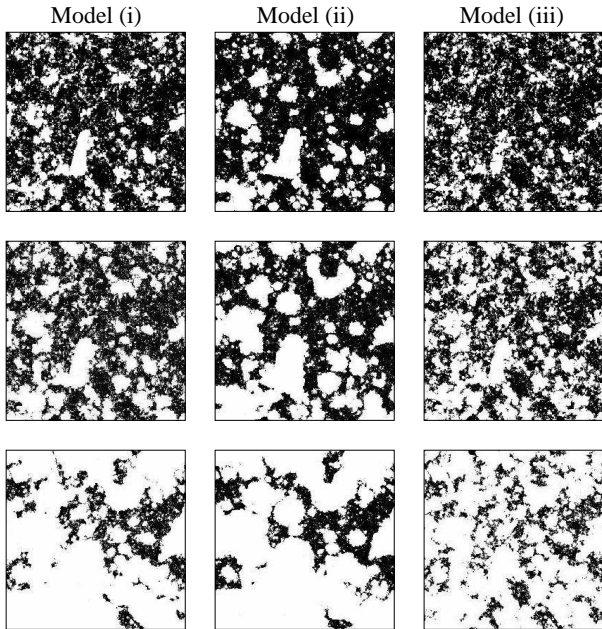


Figure 2. Slices through the middle of the simulation box for the three models discussed in the text, each with width 186 Mpc and with $6.9 < z < 8.5$. The white regions are fully ionised and the black are fully neutral. The top row uses snapshots with volume-weighted neutral fractions of $\bar{x}_H = 0.7$, the middle uses those with $\bar{x}_H = 0.5$, and the bottom uses those with $\bar{x}_H = 0.2$.

Model (iii): Absorption by minihalos shapes the morphology of reionisation and $\dot{N}_{\text{ion}} \sim m$ for $m > m_{\text{cool}}$. All minihalos with $m > 10^5 M_\odot$ absorb incident ionising photons out to their virial radii until they are photo-evaporated. We use the fitting formula for the evaporation timescale given in Iliev et al. (2005). This timescale is roughly the sound-crossing time of a halo, or $t_{\text{ev}} = 100 (m/10^7 M_\odot) \text{ Myr}$ (Shapiro et al. 2004).

The normalisation of the function $\dot{N}_{\text{ion}}(m)$ in the three simulations is chosen such that reionisation is completed by $z \approx 7$. Given the uncertainties in f_{esc} – the fraction of ionising photons that escape and ionise the IGM – and in the SFR in high-redshift galaxies, there is a large range of possible normalisations. Fortunately, the morphology of reionisation when comparing at fixed \bar{x}_H depends only weakly on the normalisation of \dot{N}_{ion} , as shown in McQuinn et al. (2007a). McQuinn et al. (2007a) and McQuinn et al. (2007b) also showed that other effects such as thermal feedback on sub-Jeans mass galaxies, source duty cycle, and the number of recombinations have negligible impact on the morphology for reasonable models. In fact, studies have demonstrated that the morphology of reionisation is shaped principally by the clustering of the ionising sources (Furlanetto et al. 2004a,b, 2005; Zahn et al. 2007; McQuinn et al. 2007a).

Figure 2 displays slices through simulations adopting reionisation models (i), (ii), and (iii). The white regions are ionised and the black are neutral. Model (ii) results in the largest HII regions because it has the most biased sources, whereas model (iii) produces the smallest bubbles, with the maximum bubble radius restricted to be roughly the mean free path for ionising photons to intersect a minihalo.

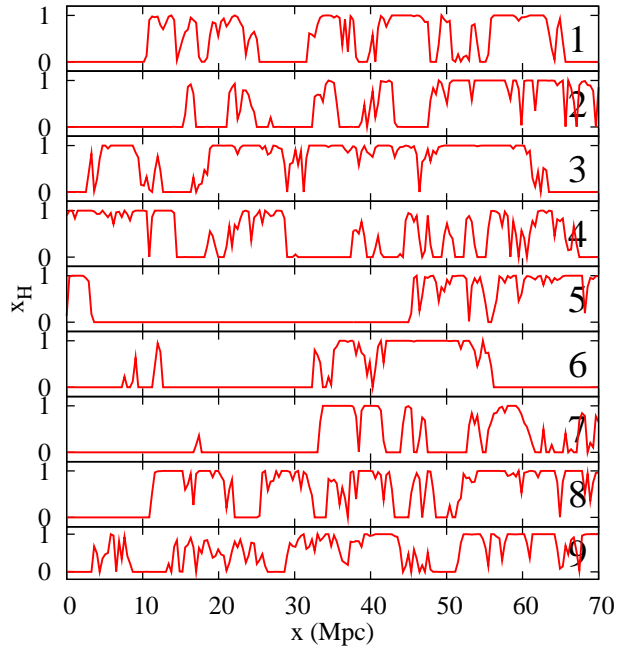


Figure 3. Nine randomly selected 70 Mpc skewers originating at a GRB in the simulation volume. These sight-lines are chosen from a snapshot from the simulation of model (i) that has $\bar{x}_H = 0.5$ and is from $z = 7.3$.

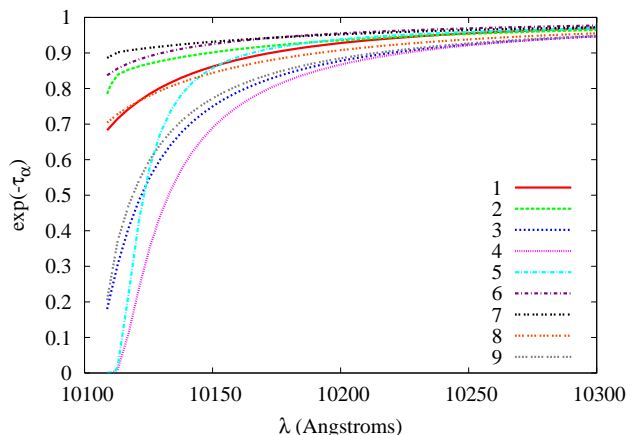


Figure 4. Transmission for the nine skewers displayed in Figure 3. Each transmission curve is calculated from the sight-line in Figure 3 that bears the same number.

The absorption profile of a GRB afterglow probes a line of sight through the IGM. Most of the absorption from the IGM occurs at < 70 Mpc from the host galaxy, and the neutral regions in the IGM that lie closer to the GRB contribute more absorption than those further away. It is clear from Figure 2 that different sight-lines encounter vastly different spatial distributions of x_H . To further illustrate this point, Figure 3 displays nine randomly selected 70 Mpc skewers originating at a potential GRB site in the simulation volume. These skewers are from the $z = 7.3$ snapshot of the simulation using model (i) for which the volume-averaged neutral fraction is $\bar{x}_H = 0.5$ and the mass-averaged neutral fraction

is 0.4.⁵ Henceforth, \bar{x}_H refers to the volume-averaged neutral fraction. To assign locations for GRBs in the simulation volume, we assume that the \dot{N}_{ion} of a halo is proportional to the GRB rate (which is true if the GRB rate traces the massive SFR and f_{esc} is independent of halo mass).

Figure 4 plots the IGM transmission redward of Ly α for the nine GRB sight-lines shown in Figure 3. To compute these curves, we use Equation (1) and the density, ionisation, and velocity fields from the simulation. The observed transmission across these six lines of sight varies enormously, and this variance needs to be accounted for in measurements of \bar{x}_H using GRBs. These calculations do not account for the evolution in \bar{x}_H along the line of sight owing to light-travel effects, but instead compute the absorption from a skewer using a snapshot that is fixed in time. In the time for light to travel 50 Mpc, the value of \bar{x}_H in the simulations of model (i) changes by 0.06, 0.08, and 0.13 when $\bar{x}_H = 0.7, 0.5$, and 0.2, respectively. A proper treatment of the evolution of \bar{x}_H along a sight-line would hardly affect our conclusions.

For the nine sight-lines in Figure 3, the best fit (\bar{x}_H, R_b) to the afterglow transmission redward of Ly α are respectively (0.31, 6.6), (0.35, 14), (0.47, 2.3), (0.51, 0), (0.28, 0), (0.21, 10), (0.32, 22), (0.45, 10), and (0.43, 2.5).⁶ While these two parameters do not fully characterise the distribution of \bar{x}_H , the actual value for R_b of the GRB host bubble corresponds roughly to the size given by these fits and the fitted value for \bar{x}_H is within 0.3 of the global value. In reality, a DLA will also affect the damping wing profile, and its absorption must be accounted for simultaneously. We incorporate this extra complication in the following section.

The top left panel in Figure 5 plots the probability distribution of GRB host HII bubble radii, $P(R_b)$. The GRB host bubble radius is defined as the distance it requires for a skewer to cross three simulation grid cells that are more than 1% neutral. The dashed, solid, and dot-dashed curves are $R_b P(R_b)$ for $\bar{x}_H = 0.2, 0.5$ and 0.7, respectively. The thick curves are for model (i), and the medium width and thin solid curves (shown only for $\bar{x}_H = 0.5$) adopt model (ii) and model (iii), respectively. These curves demonstrate that the function $P(R_b)$ depends more strongly on \bar{x}_H than on the reionisation model. When $\bar{x}_H \approx 0.5$, the typical GRB resides in a bubble of size $R_b \approx 10$ Mpc, and when $\bar{x}_H \approx 0.2$ this number increases to $R_b \approx 60$ Mpc.

The top right panel in Figure 5 shows the distribution of \bar{x}_H along the line of sight to a GRB at fixed global \bar{x}_H . To create this PDF, we generate 10^6 skewers that originate at GRBs in the simulation volume and then tabulate \bar{x}_H along each skewer, weighting points as $1/r^2$ where r is the distance from the source – roughly the same weighting that is relevant to the damping wing optical depth at observed

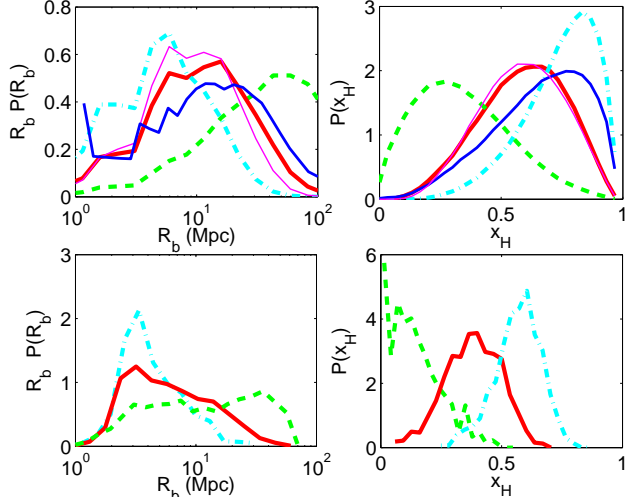


Figure 5. Dashed, solid, and dot-dashed curves represent $\bar{x}_H = 0.2, 0.5$ and 0.7, respectively. The thick curves are calculated using model (i), and, in the top panels, the medium width and thin solid curves (shown only for $\bar{x}_H = 0.5$) use model (ii) and model (iii). *Top Left Panel:* The PDF of R_b constructed from 10^6 sight-lines, in which R_b is defined as the length of a skewer originating at a GRB that passes through three grid cells with $x_H > 0.01$. *Top Right Panel:* The PDF of \bar{x}_H measured directly from 10^6 lines of sight as discussed in the text. *Bottom Panels:* The same as the top panels except that the PDFs of x_H and R_b are constructed from fitting the afterglow transmission curves computed from 1000 different simulation sight-lines with these parameters.

frequency $\nu_\alpha/(1 + z_g)$ (eqn. 2). We do not include points inside the host bubble in this tabulation.

The wide breadth of the \bar{x}_H distributions indicate that a single GRB cannot be used to directly measure the global value of \bar{x}_H to a precision of $\delta\bar{x}_H \approx 0.3$. Despite the scatter in \bar{x}_H , a single GRB can be used to detect whether the IGM is neutral. We focus on the probability of a GRB allowing the detection of reionisation in the next section.

It is possible that GRBs occur in only the most massive galaxies (rather than in a typical one, as we have assumed thus far). If only halos with $m > 10^{10} M_\odot$ are able to produce GRBs with a rate proportional to the halo mass, again weighting these halos by their SFR, we find that the average bubble size increases by a comparable amount to the size increase between model (i) and model (ii) shown in Figure 5. However, we find that the low-end tail of $P(R_b)$ starts to disappear with increasing m , even though the peak of the PDF does not shift significantly.

Thus far, we have discussed the distribution of \bar{x}_H and R_b measured directly from the simulations. For a GRB afterglow, \bar{x}_H and R_b are measured by fitting these parameters to the afterglow damping wing (even though this parameterisation for the distribution of x_H along a sight-line is highly simplified). The bottom panels in Figure 5 show the PDF of R_b and \bar{x}_H from fits to 1000 transmission curves computed from GRBs in the simulation of model (i). We ignore the effect of DLA absorption in these fits. These PDFs are notably different from those in the top panels – favouring smaller R_b and lower \bar{x}_H . While this procedure returns biased values for R_b and \bar{x}_H relative to the values we estimate

⁵ The ionisation fronts are much narrower than our grid size for reionisation by POP-II-like stars (as is assumed in these simulations). Resolution effects smear out the simulation ionisation field, making it deviate from a field of 0s and 1s. This smearing does not appreciably affect the results of the calculations reported here.

⁶ Note that the two skewers which are best fit with $R_b = 0$ are anomalous, and the total fraction of lines of sight that are best fit with $R_b = 0$ is a much smaller fraction than suggested by this sample of nine sight-lines.

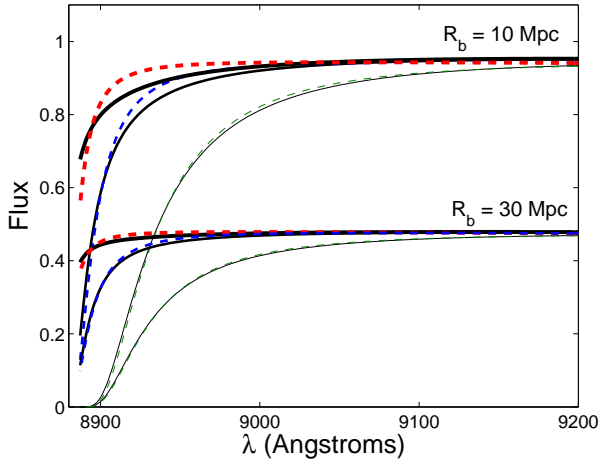


Figure 6. Afterglow spectrum of a hypothetical $z = 6.3$ burst, computed with $\bar{x}_H = 0.5$ and $N_{\text{HI}} = 10^{19} \text{ cm}^{-2}$ (thick solid curves), $N_{\text{HI}} = 10^{20} \text{ cm}^{-2}$ (medium-width solid curves), and $N_{\text{HI}} = 10^{21} \text{ cm}^{-2}$ (thin solid curves) for the specified R_b . The dashed curves are the best fits for a model that includes only DLA absorption, fitted to $\Delta\lambda = 200 (1 + z_g) = 1500 \text{ \AA}$. The normalisation of the two sets of curves is adjusted to aid viewing.

in the top panel, we find that this two parameter model provides an excellent fit to the absorption profile (as we discuss in Section 4).

4 FITTING THE DAMPING WING IN GRBS

This section quantifies the circumstances under which a GRB afterglow can be used to detect a neutral IGM. Previous sections have illustrated how the patchiness of the IGM and the strength of the host DLA complicate this measurement. In addition, there are other uncertainties such as the power-law slope and amplitude of the intrinsic GRB spectrum, the precise redshift of the GRB and of the DLA, and dust absorption and metal line contamination from the host galaxy or from intervening systems. A systematic discussion of these issues is presented in Totani et al. (2006). To rule out an ionised IGM with a GRB afterglow, a multi-parameter fit to its spectrum that assumes an ionised IGM and that accounts for the aforementioned uncertainties must provide a poor fit.

4.1 Fits to a Toy Absorption Model

A toy example of such a multi-parameter fit that accounts for some of these uncertainties is shown in Figure 6. In this figure, the simple case of a bubble with size R_b in a homogeneous IGM with neutral fraction \bar{x}_H is shown. The solid curves are absorption models that have the intrinsic parameters $\beta = 1.25$, $z_g = z_{\text{DLA}} = 6.3$,⁷ $\bar{x}_H = 0.5$ and $N_{\text{HI}} = 10^{19} \text{ cm}^{-2}$ (thick curves), $N_{\text{HI}} = 10^{20} \text{ cm}^{-2}$

(medium-width curves), or $N_{\text{HI}} = 10^{21} \text{ cm}^{-2}$ (thin curves).⁸ We then fit to these model curves. Our fitting weights all frequency bins equally. The presence of night-sky OH lines and the wavelength dependence of the CCD sensitivity should make the weighting slightly non-uniform in a real observation.

The dashed curves in Figure 6 are fits over $\Delta\lambda = 200 (1 + z_g)$ to a model that only include DLA absorption. This model fits for the parameters N_{HI} , β , and A . The absorption owing to a substantially neutral IGM is more easily fit with *just* a DLA model as R_b increases or as N_{HI} increases. If we had fit over a larger $\Delta\lambda$, the dashed and solid curves would differ by less at wavelengths where the absorption is important. The fits in Figure 6 assume that z_{DLA} is known from metal lines, as was the case for GRB050904. For GRBs in more metal-poor galaxies or for GRBs with smaller DLAs, this may not always be possible. When fits include z_{DLA} as a free parameter, a neutral IGM is much harder to distinguish from an ionised one (Barkana & Loeb 2004).

To quantify the capability of distinguishing different absorption models, we define the measure

$$\langle \Delta\chi^2 \rangle = \sum_{i=1}^N \frac{[F_2(\lambda_i) - F_1(\lambda_i)]^2}{\sigma(\lambda_i)^2}, \quad (3)$$

where F_1 and F_2 are the afterglow fluxes for models 1 and 2. This quantity represents the average difference in χ^2 between two models for a spectrum that has noise $\sigma(\lambda_i)$ in channel λ_i and that has N wavelength channels, assuming the data is drawn from model 1 or 2.

When comparing a model with a neutral IGM to an ionised one, two models can be distinguished at X confidence level (C.L.) if X of the total likelihood is contained between the maximum likelihood in the neutral IGM model and $\exp[-\langle \Delta\chi^2 \rangle / 2]$ of that likelihood value (assuming Gaussianity). For a 4 parameter fit, two models that differ by $\langle \Delta\chi^2 \rangle = 8$ signifies that model 1 is, in the mean, preferred at 91% C.L. over model 2 ($\langle \Delta\chi^2 \rangle = 5$, 70% C.L. and $\langle \Delta\chi^2 \rangle = 12$, 98% C.L.). The significance levels at fixed $\Delta\chi^2$ for fits with three and five parameters are similar. In what follows, we quote $\langle \Delta\chi^2 \rangle$ in terms of $\Delta\lambda_i = 3 \text{ \AA}$ and $\sigma_{\mathcal{F}} = 0.1$, where $\Delta\lambda_i$ is the width of a frequency channel and $\sigma_{\mathcal{F}}$ is the standard deviation in the flux in each spectral channel in units of A . These are approximately the values of $\Delta\lambda_i$ and $\sigma_{\mathcal{F}}$ for the Subaru FOCAS spectroscopic observation of GRB050904.

First, we consider the case in which the absorption spectrum is parameterised by $N_{\text{HI}} \approx 10^{19} \text{ cm}^{-2}$, $\bar{x}_H = 0.5$, and $R_b = 10 \text{ Mpc}$ (similar to the fits in Fig. 6).⁸ We fit to $\Delta\lambda = 50 (1 + z_g) \text{ \AA}$ redward of source-frame Ly α . This fit results in $\langle \Delta\chi^2 \rangle = 5 \times (3 \text{ \AA} / \Delta\lambda_i) \times (0.1 / \sigma_{\mathcal{F}})^2$ between the model for a neutral IGM and the model for an ionised IGM. Next, we fit to a model with the same specifications as the previous fit but with $N_{\text{HI}} \approx 10^{20} \text{ cm}^{-2}$ [$N_{\text{HI}} \approx 10^{21} \text{ cm}^{-2}$].

⁷ The assumption that $z_g = z_{\text{DLA}}$ is probably reasonable for GRBs in high-redshift galaxies, where the circular velocity of these halos is typically $\sim 25 \text{ km s}^{-1}$ (Barkana & Loeb 2004).

⁸ We include the prior $0.75 < \beta < 1.75$ in the fits: β will likely be constrained by earlier photometric observations redward of the absorption, as was the case for GRB050904 (Totani et al. 2006). In addition, we exclude wavelengths within 400 km s^{-1} of the host galaxy because such regions could be affected by Ly α emission from the galaxy as well as resonant absorption by infalling material.

This fit results in $\langle \Delta\chi^2 \rangle = 3 [0.2] \times (3\text{\AA}/\Delta\lambda_i) \times (0.1/\sigma_{\mathcal{F}})^2$. Therefore, $\Delta\lambda_i \lesssim 3\text{\AA}$ and $\sigma_{\mathcal{F}} \lesssim 0.1$ are required for any hope of detecting a neutral IGM for the $N_{\text{HI}} \approx 10^{19}\text{ cm}^{-2}$, $x_H \approx 0.5$, and $R_b = 10\text{ Mpc}$ case, and even better sensitivity is required for the other two examples.

Let us investigate how the quoted $\langle \Delta\chi^2 \rangle$ depend on the assumptions we have made. For this discussion, we again assume an absorption model with $\bar{x}_H = 0.5$, $R_b = 10\text{ Mpc}$, and $N_{\text{HI}} \approx 10^{20}\text{ cm}^{-2}$, and we assume a measurement with $\Delta\lambda_i \approx 3\text{\AA}$ and $\sigma_{\mathcal{F}} \approx 0.1$.

- If we restrict β to $1.0 < \beta < 1.5$ (rather than to $0.75 < \beta < 1.75$, as before), $\langle \Delta\chi^2 \rangle$ increases from 3 to 4. If we fix $\beta = 1.25$, then $\langle \Delta\chi^2 \rangle = 5$.
- If we allow z_{DLA} to vary and fix $\beta = 1.25$, $\langle \Delta\chi^2 \rangle$ decreases to 1.
- If we instead fit the first $\Delta\lambda = 200 (1 + z_g)\text{\AA}$ redward of $\text{Ly}\alpha$ rather than $\Delta\lambda = 50 (1 + z_g)\text{\AA}$, $\langle \Delta\chi^2 \rangle$ increases from 3 to 6.

The increase in $\langle \Delta\chi^2 \rangle$ with bandwidth owes to tighter constraints on A and β , the parameters that determine the spectrum far redward from the $\text{Ly}\alpha$ absorption feature. These tighter constraints breaks degeneracies between these parameters and the parameters that determine the absorption. The appropriate choice of bandwidth will not always be clear-cut; fits should not include wavelengths where the dust absorption, the instrumental response, and other factors are not understood to better than the difference between the two absorption models. Already for $\Delta\lambda \approx 300\text{\AA}$, such calibration is necessary to the 1% level (Fig. 6). In addition, even uncertainties in the cosmological parameters make a difference in distinguishing models at the percent level (Miralda-Escude 1998).

4.2 Fits to the Simulated Absorption Spectra

Thus far, we have considered fits to a toy model for IGM absorption. To realistically model IGM absorption we calculate mock spectra from simulation skewers of reionisation model (i) and we set $\beta = 1.25$. We fit this mock data with different absorption models in what follows.

Despite the complicated distribution of neutral hydrogen along sightlines, a simple model with just the parameters R_b and \bar{x}_H (in addition to parameters that account for DLA absorption and the intrinsic afterglow spectrum) typically provides an excellent fit to the mock data. This is surprising because of the highly simplified nature of this model. The $\langle \Delta\chi^2 \rangle$ between the true model – the absorption profile calculated from the simulation – and the best fit neutral IGM model, which fits for R_b and \bar{x}_H , typically range between $10^{-3} - 10^{-7} \times (3\text{\AA}/\Delta\lambda_i) \times (0.1/\sigma_{\mathcal{F}})^2$ for $N_{\text{HI}} = 10^{20}\text{ cm}^{-2}$. These small values mean that $\sigma_{\mathcal{F}} \approx 10^{-2} - 10^{-4}$ is required to rule out this 2-parameter IGM absorption model (measurements $\approx 10 - 1000$ times more sensitive than those for GRB050904).

Figure 7 shows the distribution of $\langle \Delta\chi^2 \rangle$ between fits to the simulated spectra with the parameters R_b , \bar{x}_H , N_{HI} , A and β versus fits with just the last three parameters (i.e., a DLA and an ionised IGM). These fits are to a wavelength interval that spans $50 (1 + z)\text{\AA}$ redward of rest-frame $\text{Ly}\alpha$. If the fits with $\bar{x}_H = 0$ are disfavoured by the data (i.e., if $\langle \Delta\chi^2 \rangle \gtrsim 8$), then a neutral IGM will

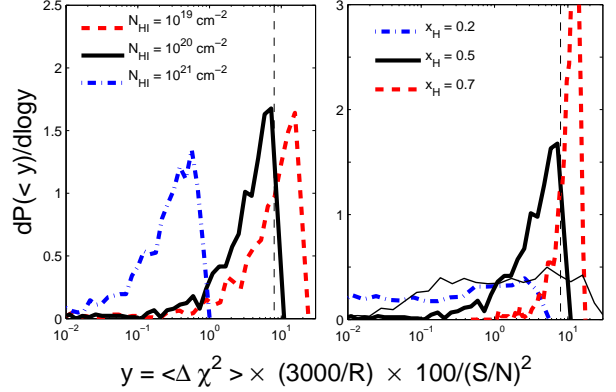


Figure 7. PDFs of $\langle \Delta\chi^2 \rangle$, where $\langle \Delta\chi^2 \rangle$ is the average difference in χ^2 between the “true” model (which fits \bar{x}_H and R_b) and a model with only DLA absorption. These PDFs are generated by fitting 1000 sight-lines from the simulation of model (i) at the specified \bar{x}_H . Note that the parameter y that is plotted on the abscissa is scaled to be independent of S/N and R . The left panel shows the dependence of the PDF on N_{HI} , using spectra from a snapshot with $\bar{x}_H = 0.5$, and the thick curves in the right panel show the dependence on \bar{x}_H , assuming $N_{\text{HI}} = 10^{20}\text{ cm}^{-2}$. The thin black curve in the right panel folds in the observed distribution of N_{HI} and uses spectra with $\bar{x}_H = 0.5$. A neutral IGM is detected on average at $> 84\%$ confidence level when $\langle \Delta\chi^2 \rangle > 8$ (marked by the vertical dashed lines for $R = 3000$ and $S/N = 10$).

be favoured by the data. The parameter y that is plotted on the abscissa in Figure 7 is scaled to be independent of S/N (we define $S/N \equiv \sigma_{\mathcal{F}}^{-1}$) and spectrograph resolution R ($R \equiv \lambda_i/\Delta\lambda_i$). For an observation like the FOCAS observation of GRB050904 ($R = 3000$ and $S/N = 10$), a DLA with $N_{\text{HI}} \lesssim 10^{20}\text{ cm}^{-2}$ is needed to have a good chance of detecting a neutral IGM when $\bar{x}_H \approx 0.5$ (left panel in Fig. 7). For $\bar{x}_H < 0.5$, a higher signal-to-noise measurement is required.

The results in Figure 7 depend on the parameters we fit as well as the wavelength range included in the fit. If we fix the parameter $\beta = 1.25$ instead of fitting for it, the PDFs in this figure are, for the most part, unchanged. If we fit a larger range in wavelength of $\Delta\lambda = 200 (1 + z)\text{\AA}$, the fits improve slightly – shifting the histogram by factor of ≈ 1.5 .

The thin solid curve in the right panel of Figure 7 is the PDF of $\langle \Delta\chi^2 \rangle$ for spectra computed for $\bar{x}_H = 0.5$ and where we have folded in the distribution of DLA N_{HI} values observed in lower redshift GRB-host systems. We assume that the cumulative distribution of DLAs is a power-law of the form $N_{\text{HI}}^{0.3}$ for $N_{\text{HI}} < 10^{21.5}\text{ cm}^{-2}$, which is consistent with observations (Chen et al. 2007). Half of GRB DLAs have $N_{\text{HI}} > 10^{21.5}\text{ cm}^{-2}$, but we do not include these bursts in this computation. These bursts will contribute to the small $\langle \Delta\chi^2 \rangle$ tail of the PDF.

Let us assume there exists an observation with similar sensitivity to the Subaru FOCAS spectrum of GRB050904, that the distribution of DLAs is the same as found at lower redshift, that the redshift of the GRB is known via metal lines, and that the GRB originates from a redshift at which $\bar{x}_H \approx 0.5$. The spectrum of this GRB can be used to detect a partly neutral IGM at 97% C.L. ($\langle \Delta\chi^2 \rangle > 12$) approximately 5% of the time (and, for an observation with

3 times the sensitivity, $\approx 25\%$ of the time) if the fit uses $\Delta\lambda = 50 (1+z) \text{ \AA}$.⁹ If the fit uses $\Delta\lambda = 200 (1+z) \text{ \AA}$, this becomes $\approx 10\%$ of the time (and, for an observation with 3 times the sensitivity, $\approx 30\%$ of the time).

An earlier spectroscopic pointing could result in higher S/N values than the fiducial value of 10 because the optical afterglow fades as a power-law in time with slope ≈ -1.2 (Liang & Zhang 2006). The same Subaru observation taken ≈ 8 hr after GRB050904 would have resulted in $10\times$ the sensitivity and a detection of reionisation the majority of the time. In 2013, JWST is projected to be in orbit. Let us assume a $z = 8$ GRB is observed with a 10^4 s integration using the JWST spectrograph NIRSspec operating in its highest resolution mode of $R = 2700$. To detect the GRB with $S/N = 10$ in each frequency channel requires a minimum flux of $F(\lambda) = 2 \times 10^{-19} \text{ erg cm}^{-2} \text{ s}^{-1} \text{ \AA}^{-1}$.¹⁰ This minimum flux is approximately five times the sensitivity of the Subaru FOCAS observation of GRB050904. However, while ground based observations can potentially target GRB afterglows minutes after their trigger, JWST will only be able to slew to high-redshift afterglows ~ 1 day after the burst (Gardner et al. 2006).

Even though the calculations in this section were for $z \approx 6-8$, similar conclusions hold for higher redshifts reionisation scenarios. The amount of absorption does increase with increasing z_g because the damping wing optical depth scales as $\approx (1+z_g)^{3/2}$ (eqn. 2). However, the morphology of reionisation depends weakly on redshift for stellar reionisation scenarios – bubbles have a similar comoving size distribution at a fixed \bar{x}_H independent of when reionisation happens (McQuinn et al. 2007a). For reasonable redshifts over which reionisation could occur, the amount of damping wing absorption predicted by our simulations is similar and our conclusions do not change.

As a final point, the distribution of the best-fit R_b and \bar{x}_H from the fits that include DLA absorption are very similar to the distribution in Figure 5 in which the effect of a DLA was ignored. Therefore, the presence of a DLA does not significantly bias the best fit values for R_b and \bar{x}_H .

5 GRB050904

The $z = 6.3$ GRB, GRB050904, is the burst with the highest identified redshift (Kawai et al. 2006; Haislip et al. 2006; Totani et al. 2006). A 4 hour observation of this burst was taken using the FOCAS spectrograph on Subaru 3.4 days after the prompt gamma ray emission. The spectrum from this observation is shown in Figure 8. Totani et al. (2006) showed that this spectrum is well-fitted with a DLA of column density $N_{\text{HI}} \approx 10^{21.6} \text{ cm}^{-2}$ and that this GRB disfavours additional absorption owing to a neutral IGM, deriving the constraint $\bar{x}_H < 0.6$ at 95% C.L. This section investigates the constraints on \bar{x}_H from GRB050904 if a patchy reionisation process consistent with simulations is taken into account.

First, we have re-performed the analysis of Totani et al. (2006), accounting for galactic absorption of $E(B-V) = 0.06$ and masking the same regions of the spectrum as in

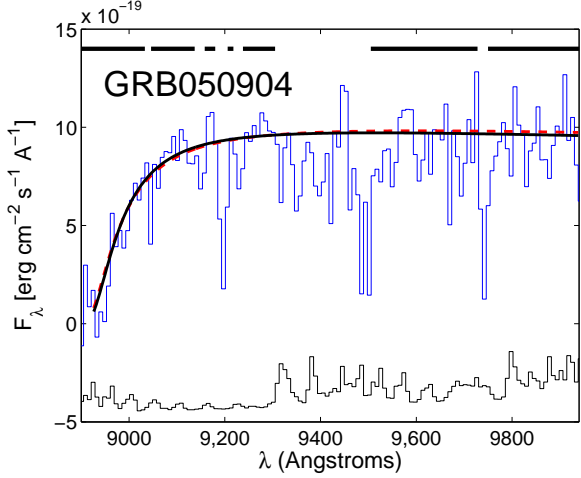


Figure 8. Binned afterglow spectrum of GRB050904 (each 2.67 \AA wavelength channel has been binned into 8 \AA pixels), as well as the best fit models for $x_H = 0$ (solid curve) and $x_H = 1$ (dashed curve). The bottom curves are the $1\text{-}\sigma$ errors on each binned pixel with an offset of -5×10^{-19} , and the thick horizontal lines at the top of the figure indicate the wavelengths that were included in the fits. Both fits require a DLA with column density $N_{\text{HI}} \approx 10^{21.5} \text{ cm}^{-2}$.

Totani et al. (2006) because of metal line contamination. (The thick horizontal lines at the top of Figure 8 indicate the wavelength ranges that were fit.) The solid absorption curve in Figure 8 is the best fit for an ionised IGM ($\bar{x}_H = 0$) with a DLA and the dashed curve is the best fit with a DLA plus a *fully* neutral IGM. Both fits to the spectrum employ the same estimated errors as in Totani et al. (2006) and minimise χ^2 with two parameters, N_{HI} and A , holding all other parameters fixed. In particular, we fix $\beta = 1.25$ as was done in Totani et al. (2006). This value for β is consistent with $\beta = 1.25 \pm 0.25$, which was derived in Tagliaferri et al. (2005) and is consistent with the value derived in Kann et al. (2007) from all publicly available data.¹¹ The value of $\Delta\chi^2$ is not significantly changed if we instead fit with β adopting the prior $1.0 < \beta < 1.5$ (the best fit for both models then prefers $\beta = 1$), and $\Delta\chi^2$ shrinks significantly if no prior is placed on β .¹²

The χ^2 values for the two models displayed in Figure 8 are 277.3 for the ionised model and 287.0 for the neutral

¹¹ The Tagliaferri et al. (2005) value for β was derived from photometric observations with the Very Large Telescope taken 1.2 days after the prompt emission. Totani et al. (2006) argued that the softness of the β derived in Tagliaferri et al. (2005) indicates that β was determined by the power-law index of the electrons and, therefore, should not evolve significantly between the time of the measurement from Tagliaferri et al. (2005) and their measurement (i.e., other breaks in the synchrotron spectrum are at longer wavelengths).

¹² If we ignore photometric constraints on β and just fit it as a free parameter, the ionised IGM model prefers $\beta = -0.6$ at 98% C.L. ($\Delta\chi^2 = 10$) over a model with $\beta = 1.25$. While it is hard to imagine β evolving to this small value from $\beta = 1.25$, this nevertheless may indicate that there is a problem with the model for the data. Fits to the spectrum that do not place a prior on β do not prefer ionised IGM models over neutral ones.

⁹ These numbers assume that bursts with $N_{\text{HI}} > 10^{21.5} \text{ cm}^{-2}$ do not provide a positive detection of a neutral IGM.

¹⁰ <http://www.stsci.edu/jwst/instruments/nirspec/>

case.¹³ Even though these two 3-parameter models are difficult to distinguish visually, it is the case that $\Delta\chi^2 = 9.7$, which at face value implies that the ionised model is preferred over the neutral model at 98% C.L. (Totani et al. 2006). Interestingly, much of the contribution to $\Delta\chi^2$ between the neutral and ionised models comes from wavelengths that are not significantly affected by IGM and DLA absorption. If we tabulate $\Delta\chi^2$ for the best fit models in Figure 8, only including the wavelengths within 200 Å of Ly α – the wavelengths most affected by absorption – in the summation, the two model fits differ by $\Delta\chi^2 = 4$. If we include 700 Å redward of Ly α , the two model fits in Figure 8 differ by $\Delta\chi^2 = 5$. The significant contribution to $\Delta\chi^2$ from redward of the Ly α absorption stems from the fact that the neutral IGM model prefers a 2.4% higher normalization to compensate for the additional effect of IGM absorptions. As a consequence, the unabsorbed part of the spectrum needs to be modelled to a relative precision of a percent over a wavelength range with $\Delta\lambda/\lambda \approx 0.1$ for a correct interpretation of the data.

To distinguish models that differ at the 2% level over hundreds of angstroms posits that intergalactic metal and sky lines have been properly masked, that the dust reddening of the Milky Way and the host galaxy has been accurately accounted for, that the relative calibration of and errors on the measured flux are accurate, and that the model for the intrinsic spectrum is correct. Totani et al. (2006) investigated many of these uncertainties and argued that the FOCAS spectrum of GRB050904 can be used to distinguish the models in Figure 8.¹⁴

The above analysis did not fit for R_b and \bar{x}_H , which must be done to place constraints on \bar{x}_H for GRBs during the Epoch of Reionisation. However, while GRB050904 may favour an ionised universe over a neutral universe, it is more difficult to place a constraint on intermediate \bar{x}_H with GRB050904, especially in light of the large bubble sizes during reionisation. If we fit a model that fixes $\bar{x}_H = 0.5$ (about as low an \bar{x}_H as is plausible at $z = 6.3$ (Lidz et al. 2007)) and $R_b = 10$ Mpc [30 Mpc] – again fitting with A and N_{HI} and fixing β –, then the $\Delta\chi^2$ between a model with an ionised universe and this model is 3.1 [2.5], which is

¹³ To emulate the results of Totani et al. (2006), the error bars have been renormalised by the factor of 0.848 from their originally estimated value such that the $\chi^2/\text{d.o.f.} \approx 1$ for the best fit ionised model, where the number of degrees of freedom (d.o.f.) equals $268 - 3$. Totani et al. (2006) uses this rescaling to correct for uncertainty in the errors. The residuals for the best fit ionised model are close to a Gaussian with the correct width after this procedure (Fig. 3 in Totani et al. 2006).

¹⁴ Totani et al. (2006) also used the transmission in the Ly β forest as an additional handle to discriminate between the best fit for a model that assumed DLA absorption and an ionised IGM and the best fit model that assumed the absorption owed *entirely* to a neutral IGM. The later fit required the redshift of the host galaxy to be significantly redward of the best fit redshift of the DLA absorption lines, which was inconsistent with the transmission in the Ly β forest. This example is a rather exceptional case, and for most bursts Ly β will not provide an additional handle. In addition, patchy reionisation allows for transmission blueward of GRB-frame Ly β . Therefore, the Totani et al. (2006) argument can be applied only when the model value for \bar{x}_H is larger than the fraction of pixels that have transmission.

not statistically significant. To place any constraint on \bar{x}_H for GRB050904, one must account for the covariance of R_b and \bar{x}_H (i.e., lower \bar{x}_H have smaller R_b). We have not taken the additional step of accounting for this covariance in our analysis because it will not lead to interesting constraints on \bar{x}_H from GRB050904. For future bursts that prefer no IGM absorption, such an analysis will be essential. In any case, accounting properly for patchy reionisation would significantly weaken the 95% C.L. constraint $\bar{x}_H < 0.6$ at $z = 6.3$ that Totani et al. (2006) derives from GRB050904.

6 THE DAMPING WING IN QSOS AND GALAXIES

GRBs are not the only beacons in which the signature of a neutral IGM can be observed in their continuum emission. Rather than wait for a high-redshift GRB to occur, hundreds of $z > 6$ galaxies and QSOs have already been found. Perhaps these objects can be used to detect a neutral IGM. However, since the observed population of QSOs and galaxies are more biased tracers of the high-redshift Universe than are GRBs (assuming that GRBs trace star formation), they sit in larger bubbles such that the damping wing absorption is smaller, on average. The effective size of an HII region for one of the known $z \approx 6$ quasars, assuming that the IGM is significantly neutral at this redshift, is predicted to be $\gtrsim 50$ Mpc. This number accounts for these rare objects being in the most overdense regions in which reionisation occurs earlier (Lidz et al. 2007). Such large HII regions make searches that target the red damping wing in the highest redshift quasars hopeless.¹⁵

Galaxies will sit in smaller HII regions than QSOs. The average bubble size around galaxies is larger than those for GRBs. As noted in §3, the difference in the typical bubble size is typically less than a factor of two between halos of $m \approx 10^{10-11} M_\odot$ (roughly the mass of halos of spectroscopically confirmed $z > 6$ galaxies) and GRB-hosting halos.

However, there are two significant complications. First, because galaxies are much fainter, the continuum emission for high-redshift galaxies is difficult to detect spectroscopically with existing facilities. Stacking galaxy spectra is necessary to have any hope of detecting a damping wing feature with current data. Another significant complication is that the continuum of galaxies is far from a simple power-law. Such uncertainties must be accounted for in any analysis that attempts to obtain \bar{x}_H from the damping wing absorption profile of a galaxy.

7 CONCLUSIONS

GRBs are the most luminous sources at high redshifts, and their smooth power-law spectra are ideal for isolating the

¹⁵ Rather than analyse wavelengths redward of the QSO Ly α line, damping wing absorption from neutral patches in the IGM would also affect the Ly α forest of these QSOs (Mesinger & Haiman 2007). Owing to little forest transmission at $z > 6$, this feature would be difficult to detect (Lidz et al. 2007).

effects of absorption owing to a neutral IGM. However, observations must separate the impact of IGM absorption from that of a DLA to detect a neutral IGM. If no damping wing feature from IGM absorption is detected in the spectrum of a high-redshift GRB, one must be careful to conclude that reionisation is complete at the redshift of interest.

We have shown that there is a wide probability distribution of HII region sizes, and that there is large variation in the distribution of \bar{x}_H along different sight-lines. A non-detection of neutral hydrogen from a GRB afterglow spectrum might arise because the GRB host galaxy sits within a large HII region. If absorption owing to a neutral IGM is detected, it will be impossible to infer \bar{x}_H from a single GRB to better than $\delta\bar{x}_H \sim 0.3$ because of the patchiness of reionisation.

Assuming an observation with similar sensitivity to the Subaru FOCAS spectrum of GRB050904, that the distribution of DLAs is the same as found at lower redshifts, and that the redshift of the GRB is known, a GRB from a redshift at which $\bar{x}_H \approx 0.5$ can be used to detect a partly neutral IGM at 98% C.L. $\approx 10\%$ of the time (and, for an observation with 3 times the sensitivity, $\approx 30\%$ of the time). If $\bar{x}_H < 0.5$, these percentiles for detection are even smaller. Weaker DLAs enhance the probability of detecting a neutral IGM, but too weak of a DLA may prevent a precise redshift determination, which is essential for tight constraints on \bar{x}_H .

Since the $z = 6.3$ burst GRB050904 has a DLA with $N_{\text{HI}} = 10^{21.6} \text{ cm}^{-2}$, the absorption on the red side of the line is dominated by the DLA (Totani et al. 2006). While this burst may favour a model with an ionised universe over a neutral universe (Totani et al. 2006), a weaker DLA is necessary to be able to constrain \bar{x}_H in the spectrum of a high-redshift GRB. This is particularly true if the GRB occurs within a large HII region.

GRB050904 was observed spectroscopically by the Subaru telescope 3.4 days after the prompt gamma ray emission. If this afterglow had been observed hours after the burst, the flux would have been more than an order of magnitude larger. To detect a neutral IGM, it is crucial for optical and near-infrared spectrographs to observe candidate high-redshift GRBs as soon as possible after the prompt gamma ray emission. A high signal-to-noise ratio is critical to distinguish IGM absorption from that arising from a DLA. Such an observing programme is worthwhile given the promise that GRBs have as probes of the epoch of reionisation.

8 ACKNOWLEDGMENTS

We would like to thank T. Totani for providing the Subaru afterglow data for GRB050904 as well as for his comments on the manuscript and for answering numerous questions about the measurement. We also thank Mark Dijkstra, Claude-André Faucher-Giguère, Alexandre Tchekhovskoi, and Hy Trac for many interesting discussions and the anonymous referee for useful comments on the manuscript. MM acknowledges support through an NSF graduate student fellowship. The authors are also supported by the David and Lucile Packard Foundation, the Alfred P. Sloan Foundation, and grants AST-0506556 and NNG05GJ40G.

REFERENCES

- Barkana R., Loeb A., 2004, *ApJ*, 601, 64
 Becker G. D., Rauch M., Sargent W. L. W., 2007, *ApJ*, 662, 72
 Bloom J. S., Kulkarni S. R., Djorgovski S. G., 2002, *AJ*, 123, 1111
 Bromm, V., & Loeb, A. 2002, *ApJ*, 575, 111
 Chen, H.-W., Prochaska, J. X., & Gnedin, N. Y. 2007, *ApJL*, 667, L125
 Ciardi B., Loeb A., 2000, *ApJ*, 540, 687
 Daigne, F., Rossi, E. M., & Mochkovitch, R. 2006, *MNRAS*, 372, 1034
 Dekel A., Woo J., 2003, *MNRAS*, 344, 1131
 Djorgovski S. G., et al., 2001, in Costa E., Frontera F., Hjorth J., eds, *GRBs in the Afterglow Era*. 218
 Filliatre P., et al., 2006, *A&A*, 448, 971
 Fryer C. L., Woosley S. E., Heger A., 2001, *ApJ*, 550, 372
 Furlanetto S. R., McQuinn M., Hernquist L., 2005, *MNRAS*, 1043
 Furlanetto S. R., Zaldarriaga M., Hernquist L., 2004a, *ApJ*, 613, 1
 Furlanetto S. R., Sokasian A., Hernquist L., 2004b, *MNRAS*, 347, 187
 Gardner J. P., et al., 2006, *Space Science Reviews*, 123, 485
 Gehrels, N., et al. 2004, *ApJ*, 611, 1005
 Grindlay J. E., The Exist Team 2006, in Holt S. S., Gehrels N., Nousek J. A., eds, *GRBs in the Swift Era Vol. 836 of AIP Conference Series*. 631–641
 Haislip J. B., et al., 2006, *Nature*, 440, 181
 Hernquist L., Springel V., 2003, *MNRAS*, 341, 1253
 Iliev, I. T., Shapiro, P. R., & Raga, A. C. 2005, *MNRAS*, 361, 405
 Kann, D. A., Masetti, N., & Klose, S. 2007, *AJ*, 133, 1187
 Kawai, N., et al. 2006, *Nature*, 440, 184
 Kauffmann G., et al., 2003, *MNRAS*, 341, 33
 Kistler, M. D., Yüksel, H., Beacom, J. F., & Stanek, K. Z. 2008, *ApJL*, 673, L119
 Lamb D. Q., Reichart D. E., 2001, *astro-ph/0109037*
 Liang E., Zhang B., 2006, *ApJL*, 638, L67
 Lidz, A., McQuinn, M., Zaldarriaga, M., Hernquist, L., & Dutta, S. 2007, *ApJ*, 670, 39
 Loeb A., Rybicki G. B., 1999, *ApJ*, 524, 527
 Mackey J., Bromm V., Hernquist L., 2003, *ApJ*, 586, 1
 Malesani, D., Covino, S., Rossi, E. M., Lazzati, D., de Luca, A., Filliatre, P., & Tagliaferri, G. 2005, *Nuovo Cimento C Geophysics Space Physics C*, 28, 515
 McQuinn M., Lidz A., Zahn O., Dutta S., Hernquist L., Zaldarriaga M., 2007a, *MNRAS*, 377, 1043
 McQuinn, M., Hernquist, L., Zaldarriaga, M., & Dutta, S. 2007b, *MNRAS*, 797
 Mesinger A., Haiman Z., 2007, *ApJ*, 660, 923
 Mesinger A., Furlanetto S. R., 2007, *astro-ph/0710.0371*
 Miralda-Escude J., 1998, *ApJ*, 501, 15
 Salvaterra, R., Campana, S., Chincarini, G., Covino, S., & Tagliaferri, G. 2008, *MNRAS*, 212
 Sari R., Piran T., Narayan R., 1998, *ApJL*, 497, L17+
 Shapiro P. R., Iliev I. T., Raga A. C., 2004, *MNRAS*, 348, 753
 Sokasian A., Abel T., Hernquist L., Springel V., 2003, *MNRAS*, 344, 607
 Sokasian A., Yoshida N., Abel T., Hernquist L., Springel

- V., 2004, MNRAS, 350, 47
Spergel D. N., et al., 2007, ApJS, 170, 377
Springel V., Hernquist L., 2003, MNRAS, 339, 312
Stanek K. Z., et al., 2006, Acta Astronomica, 56, 333
Tagliaferri G., et al., 2005, *A&A*, 443, L1
Totani T., Kawai N., Kosugi G., Aoki K., Yamada T., Iye
M., Ohta K., Hattori T., 2006, PASJ, 58, 485
Trac, H., & Cen, R. 2007, ApJ, 671, 1
Yoshida N., Bromm V., Hernquist L., 2004, ApJ, 605, 579
Zahn O., Lidz A., McQuinn M., Dutta S., Hernquist L.,
Zaldarriaga M., Furlanetto S. R., 2007, ApJ, 654, 12